Research Square

Preprints are preliminary reports that have not undergone peer review.
They should not be considered conclusive, used to inform clinical practice,
or referenced by the media as validated information.

A dissolved anion replaces gas feeds in hydrocarbon electrosynthesis

Youngku Sohn

youngkusohn@cnu.ac.kr

Chungnam National University https://orcid.org/0000-0001-5052-8960

Hyeonji Lee

Chungnam National University

Hee Sub Yun

Chungnam National University

Huieun Shim

Chungnam National University

Jaehee Shin

Chungnam National University

Lei Wang

National University of Singapore https://orcid.org/0000-0002-1931-7767

Boon Siang Yeo

National University of Singapore https://orcid.org/0000-0003-1609-0867

Hee-Joon Chun

Chungnam National University

Article

Keywords:

Posted Date: November 24th, 2026

DOI: https://doi.org/10.21203/rs.3.rs-11752706/v1

License: This work is licensed under a Creative Commons Attribution 4.0 International License.
Read Full License

Additional Declarations: There is **NO** Competing Interest.

A dissolved anion replaces gas feeds in hydrocarbon electrosynthesis

Hyeonji Lee[1,†], Hee Sub Yun[1,†], Huieun Shim[1], Jaehee Shin[1], Lei Wang[2], Boon Siang Yeo[3], Hee-Joon Chun[1,*] & Youngku Sohn[1,*]

[1]Department of Chemistry, Chungnam National University, Daejeon 34134, Republic of Korea

[2]Department of Chemical and Biomolecular Engineering, National University of Singapore, Singapore

[3]Department of Chemistry, National University of Singapore, Singapore

†These authors contributed equally. *e-mail: hjchun@cnu.ac.kr; youngkusohn@cnu.ac.kr

Electrosynthesis of hydrocarbons by Fischer–Tropsch-type chain growth has largely used CO or CO_2 gas feeds, whose C–O bonds must be broken to make surface carbon. Here we show that a dissolved anion bearing a C–S bond can supply that carbon instead. On iron foil in water under argon, thiocyanate (SCN^-), a pseudohalide of industrial effluents, is converted into C_1–C_7 alkanes and alkenes under near-ambient conditions; without it no hydrocarbon forms. Dual ^{13}C/D labelling assigns 94–99% of the carbon in the C_4–C_6 products to thiocyanate and most of the hydrogen to water, and resolves two weakly mixing carbon pools when CO is co-fed. A precursor series (KSCN ≫ thiourea ≈ KSeCN ≫ KOCN) indicates that a reducible C–S or C–Se bond, not the C≡N group, makes a donor active, and operando impedance separates light-associated rate gains from bulk heating. Soluble chalcogen–carbon donors can thus replace the gas feed of hydrocarbon electrosynthesis.

Main

Electrochemical reduction of CO and CO_2 to multicarbon products offers a sustainable route to fuels and chemicals[1,2], but two constraints remain: carbon–carbon coupling beyond C_2 is difficult, and the feedstock is almost always a gas-phase C_1 molecule (carbonate capture liquids also release CO_2 at the electrode[3]), which ties the synthesis to gas delivery. On copper, chain growth proceeds through CO dimerization and crosses over to a Fischer–Tropsch-like mechanism only at elevated temperature and pressure[4]. On iron, chain growth from CO is well established thermally[5,6], and electrochemical pathways in which water-hydrogenated CH_x

monomers propagate into long chains have now been shown across several metals[7–12]. In these systems the carbon is supplied by the gas feed.

A soluble carbon source would remove the need for a gas feed, whose low solubility in water (≈1 mM for CO and ≈33 mM for CO_2 at 25 °C) limits supply to the electrode. Thiocyanate (SCN^-) is an ambidentate pseudohalide whose carbon is locked in a C≡N triple bond and tied to sulfur through a reducible C–S bond; hard–soft character decides which end binds, and such ions can shift electrode potentials[13]. Specifically adsorbing anions change CO_2-reduction activity by modifying the interface but have not been shown to supply carbon[14,15]; thiocyanate itself has been used on copper only as a passivating additive[16], and on iron it adsorbs through nitrogen or sulfur depending on potential[17]. Sulfur poisons iron Fischer–Tropsch catalysts at high coverage and promotes olefin selectivity at low coverage[18], and the C≡N group is itself reducible at an electrode, giving methylamine, ammonia and C_1–C_2 hydrocarbons[19,20] but no chain growth. We reasoned that reductive C–S scission at an iron cathode would instead release that carbon to the surface, making surface carbon from a C–S bond rather than from the C–O bonds of CO or CO_2 (Fig. 1a).

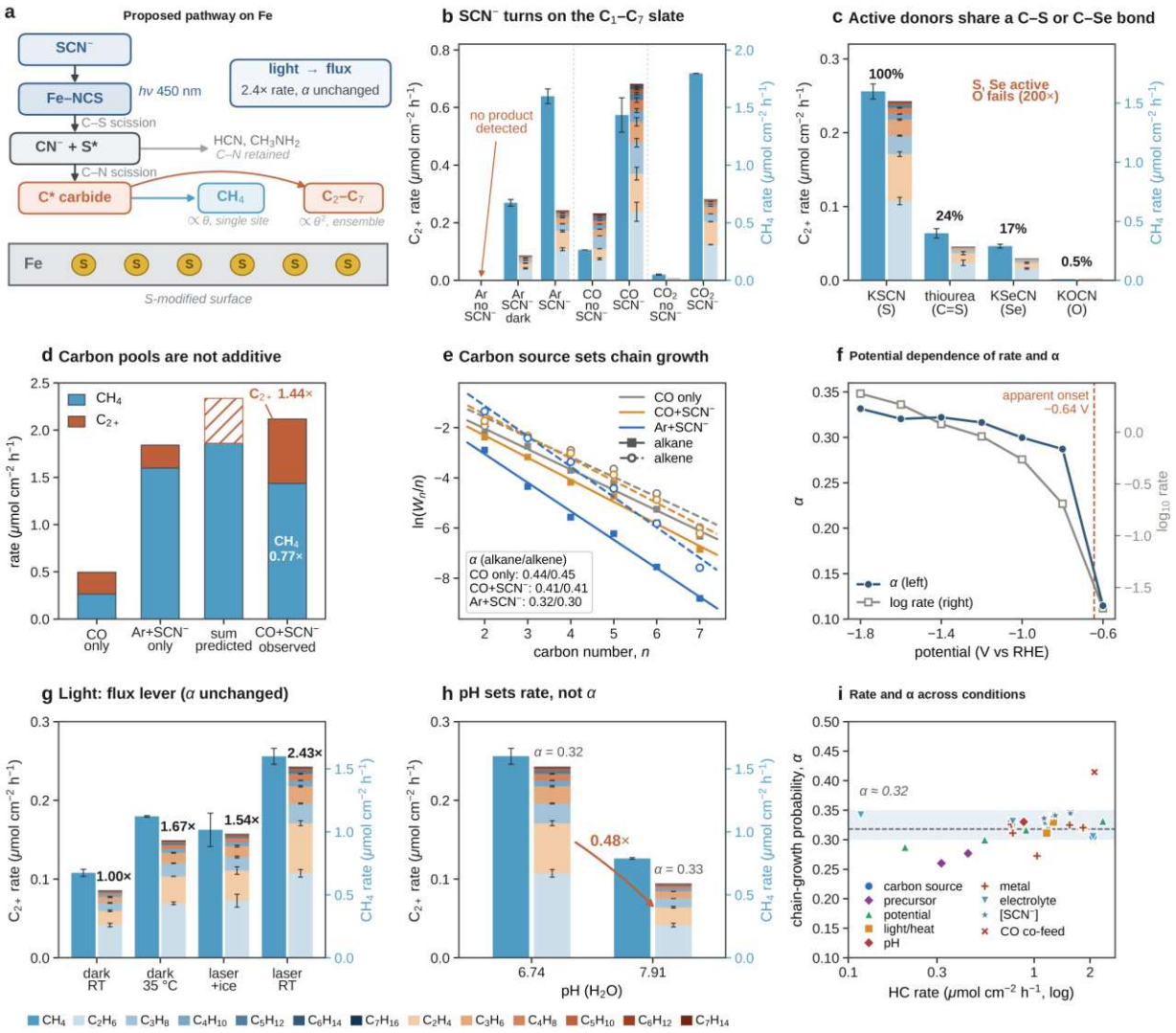
Results

Thiocyanate switches on chain growth

Under argon with no thiocyanate, an iron electrode at −1.6 V_{RHE} in 0.1 M potassium phosphate (applied; interfacial scale in Supplementary Note S9) gave no hydrocarbons above the detection limit; at open circuit neither hydrocarbons nor hydrogen were detected. Adding 0.25 mmol KSCN (5.0 mM) gave a full C_1–C_7 slate at 1.84 μmol cm^{-2} h^{-1}, methane-rich (≈87% of the hydrocarbon rate) with a chain-growth probability $\alpha \approx 0.32$ (Fig. 1b,e; Supplementary Tables S3 and S4, Supplementary Notes S1 and S2). ^{13}C labelling assigns this carbon to thiocyanate (Fig. 2c).

Visible light increases the rate but is not required: 450 nm illumination raises the dark rate (0.76 μmol cm^{-2} h^{-1} at 25 °C) 2.4×, and heating the dark cell to 35 °C raises it 1.7×. With the illuminated cell in an ice bath the gain is still 1.5× (Fig. 1g; Supplementary Note S3), so part of the light effect is not due to warming of the electrolyte; local electrode heating under the beam was not measured and remains in this light-associated gain.

Fig. 1: Thiocyanate supplies the carbon for aqueous electrochemical Fischer–Tropsch synthesis on iron.



a, Proposed mechanism: reductive C–S scission of the Fe–NCS complex, assisted by 450 nm light (tentatively through ligand-to-metal charge transfer), delivers a ∗CN/carbide fragment to the surface and leaves sulfur on it, and the carbide couples into a C_1–C_7 slate while nitrogen leaves as ammonia and the retained C–N fragment as methylamine. **b**, Product formation rates for seven conditions (Ar/CO/CO_2 × SCN^- present/absent, plus an Ar+SCN^- dark control); H_2 is omitted. The Ar/no-SCN− blank gives no carbon product; SCN^- restores a full C_1–C_7 slate (1.84 μmol cm^{-2} h^{-1}). CH_4, left bar (blue, right axis); C_{2+} slate stacked by species (alkanes blue, alkenes orange, left axis). **c,** Precursor series: only donors with a reducible C–S or C–Se bond are active (KSCN 100%, thiourea 24%, KSeCN 17%; KOCN 0.5%, ≈200-fold C–S/C–O gap). **d**, The CO+SCN^- co-feed is non-additive: C_{2+} rises to 1.44× while CH_4 falls to 0.77× of the summed single-source rates (attributed to site competition; Fig. 2). **e**, Anderson–Schulz–Flory plots resolve the pools by chain-growth probability: $\alpha_{CO} \approx 0.44$ and $\alpha_{SCN} \approx 0.32$ sit in two bands, and the co-feed (≈0.41) lies close to their weighted average (≈0.39); alkane and alkene slopes coincide within each source. **f**, Potential dependence: α (blue, left) rises through a fitted logistic midpoint at −0.64 V (applied) while the hydrocarbon rate (grey, right, log scale) rises monotonically. **g**, Illumination raises the hydrocarbon rate 2.43× at constant α; the ice-bath (≈1.5×) and 35 °C dark (≈1.7×) controls are approximately additive. **h**, Raising the bulk pH from 6.74 to 7.91 halves the rate (0.48×) at unchanged α (0.32→0.33). **i**, Master plot across eight perturbations (carbon source, precursor, potential, light/heat, pH, metal, electrolyte and [SCN^-]): above the apparent potential onset the hydrocarbon rate spans more than tenfold while α stays within 0.26–0.36 (shaded band, 0.30–0.34). The

CO + SCN^- co-feed (red), which contains the higher-α CO pool, is the only outlier. Error bars, range of duplicate electrolyses (metals in i: single runs); full datasets in Supplementary Notes S1–S9 and Supplementary Tables S2–S9.

Carbon from thiocyanate, hydrogen from water

Under argon the all-^{12}C isotopologue makes up 0–5% (mostly below 2%) of the C_4–C_7 molecular-ion clusters, which are free of interfering ions. Deconvolving each cluster against the unlabelled product and correcting for the 99 atom% reagent gives 94–99% thiocyanate-derived carbon atoms for C_4–C_6 and 88–93% for C_7, whose signal is weakest (Supplementary Table S13). The products are near-completely deuterated in D_2O (Fig. 2a–c). Ethylene formed in D_2O with ^{13}C-thiocyanate appears predominantly at m/z 34 ($^{13}C_2D_4$), so one molecule carries the thiocyanate carbon and the water hydrogen[21]. For methane, whose ions coincide with those of water and argon, the assignment rests on the argon blank and the precursor series. Under a $^{12}CO_2$ co-feed (in D_2O) the products remain ≈90% ^{13}C (85–92%), so CO_2 supplies little carbon (Supplementary Notes S2 and S7). Under 12CO the 13C content falls to ≈45% and depends on chain length (≈41% at C_4, ≈17% at C_6; C_2–C_3 values are provisional): CO contributes more carbon to longer chains (Fig. 2c,f).

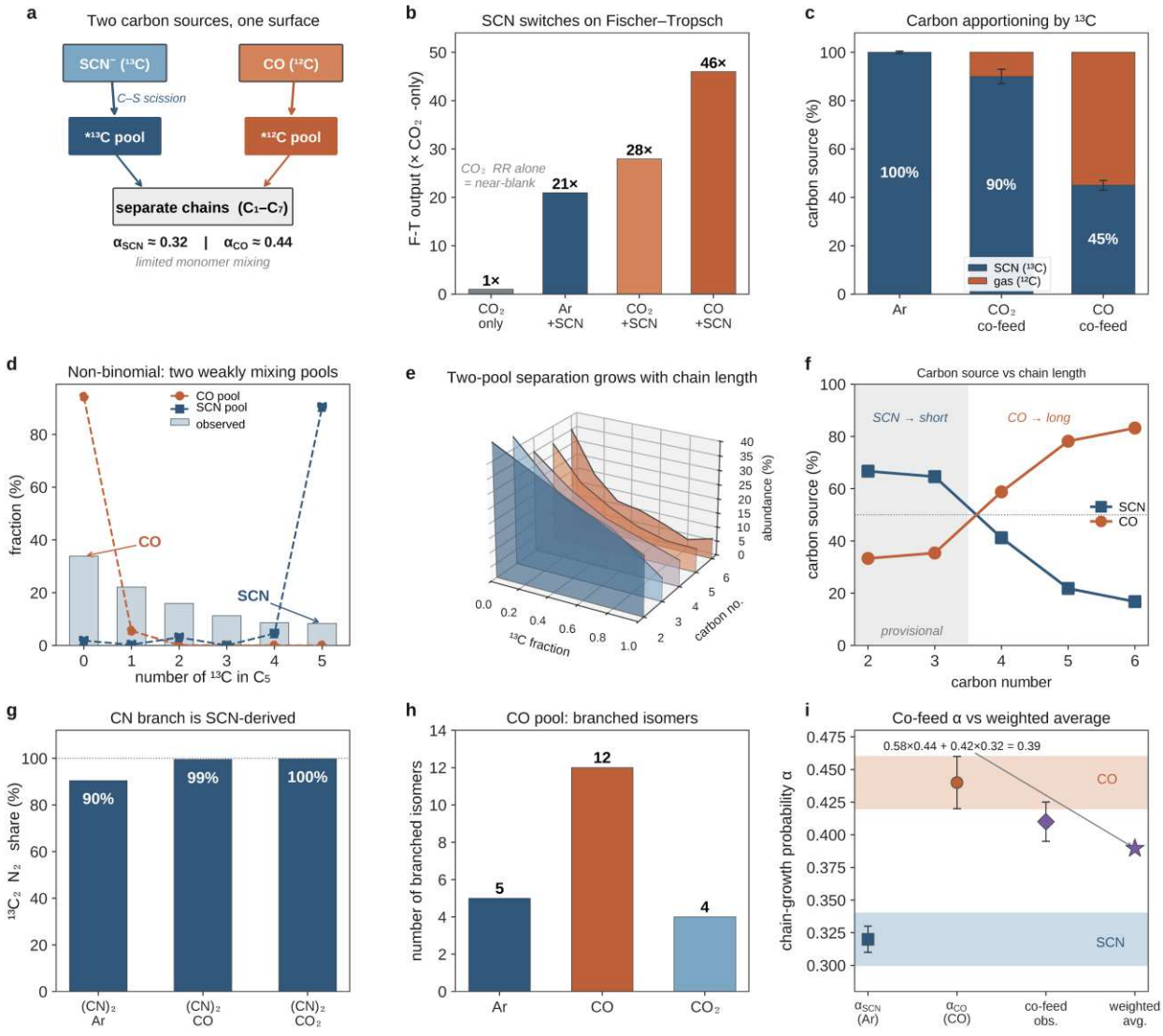
Two weakly mixing carbon pools

Iron also reduces CO on its own (α ≈ 0.44), so we asked whether the two carbon sources mix, as CO and CH_x cross-couple on copper alloys[22]. Under ^{12}CO with ^{13}C-SCN the ^{13}C isotopologue distribution of each product is broader than the single binomial expected from one mixed pool, with both the all-^{12}C and the all-^{13}C ends over-populated (Fig. 2d). A two-population model lowers the fitting residual by ≈97% (CO-derived fraction ≈58% of molecules), and the separation becomes more pronounced with chain length, thiocyanate contributing mainly to short chains and CO to long ones (Fig. 2e,f). The CO-derived fraction depends on the analysis method (Supplementary Note S14), so we use it qualitatively. Two weakly mixing pools are the simplest reading; pools separated in space or time would give a similar signature.

Cyanogen, $(CN)_2$, carries no hydrogen and is 93–100% ^{13}C in every run (99.7% under CO, 93% under argon), so CO does not enter the C≡N branch (Fig. 2g). The co-feed α (0.41 ± 0.02) lies between the two single-source values, close to their weighted average (0.58 × 0.44 + 0.42 × 0.32 ≈ 0.39; Fig. 2i). The CO co-feed also gives the most branched isomers in the $^{13}C/H_2O$ series

(Fig. 2h). We therefore attribute the non-additive rates of Fig. 1d to competition for surface sites rather than to exchange of carbon (Supplementary Note S2).

Fig. 2: Thiocyanate and CO feed two weakly mixing carbon pools.



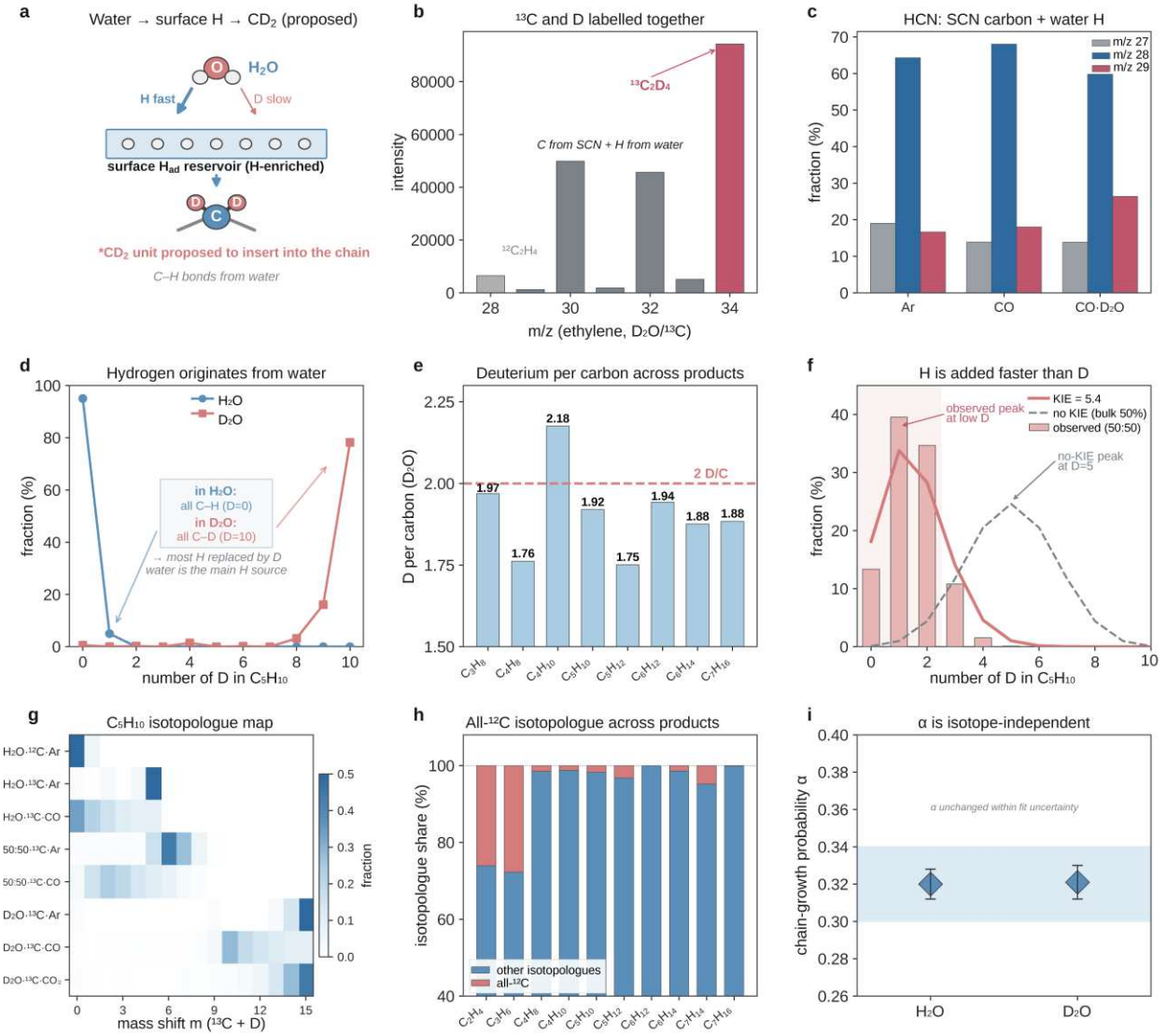
a, Thiocyanate (^{13}C, via C–S scission) and CO (^{12}C) feed two carbide pools that grow as separate chains on one iron surface. **b**, Where intrinsic CO_2 reduction is near-blank, thiocyanate switches on a full hydrocarbon slate (semi-quantitative GC–MS index: summed linear C_4–C_7 base-peak intensity relative to the CO_2-only run; Supplementary Table S12). **c**, Carbon-source fractions by ^{13}C deconvolution: ≈100% under Ar (the Ar run is the reference of the deconvolution; independently, the all-^{12}C isotopologue is 0–5% (mostly below 2%) of the C_4–C_7 clusters and the thiocyanate-derived atom fraction 94–99% for C_4–C_6, Supplementary Table S13), ≈90% under a CO_2 co-feed, ≈45% under a CO co-feed. **d**, The CO co-feed C_5 isotopologue distribution is not the single binomial expected for one mixed pool: both the all-^{12}C (CO) and all-^{13}C (SCN) ends are over-populated. **e**, Isotopologue abundance against ^{13}C fraction for C_2–C_6; the two-pool separation deepens with chain length. **f**, The CO-derived carbon fraction rises with chain length; the C_2–C_3 points are provisional because their ions overlap background ions (Supplementary Note S43). **g**, Share of cyanogen, $(CN)_2$, present as fully labelled $^{13}C_2N_2$ (m/z 54; 90–100% of the molecular ion, corresponding to 93–100% ^{13}C atoms), no lower under CO than under argon, consistent with a thiocyanate-derived

C≡N branch. **h**, Number of branched isomers in the $^{13}C/H_2O$ series; the CO co-feed gives the most. **i**, The co-feed chain-growth probability ($\alpha \approx 0.41$) lies between the single-source values, close to their weighted average ($0.58 \times 0.44 + 0.42 \times 0.32 \approx 0.39$); because a mixture of two Anderson–Schulz–Flory distributions is not itself one, this is supporting rather than primary evidence. Error bars, range of duplicate electrolyses; isotope fractions (single labelling runs), s.d. of a Poisson bootstrap over the measured ion counts, which does not include run-to-run variation. Full analysis in Supplementary Notes S10–S15, Supplementary Figs S69–S71 and S81–S103 and Supplementary Tables S12–S13.

An H-enriched surface hydrogen reservoir

In D_2O the C_4–C_6 alkenes carry 88–97% of their maximum deuterium content and the alkanes less, so most product hydrogen comes from water (Fig. 3b–e,g,h; Supplementary Notes S7 and S14); the source of the remaining protium was not identified. In 50:50 H_2O/D_2O the products contain only 11–20% D, which corresponds to a per-site H/D discrimination of 4–8, larger than the H_2O/D_2O rate ratio of 1.3–1.4 (not corrected for differences in iR drop). Hydrogenation therefore draws on adsorbed hydrogen that is enriched in H relative to the bulk solvent, plausibly the same pool that feeds hydrogen evolution, where the proton donor and interfacial water structure set the rate[23,24] (Fig. 3a,f). α is the same in H_2O and D_2O (0.320 and 0.321), so H/D substitution changes the rate without changing the measured chain-growth probability (Fig. 3i).

Fig. 3: Hydrogen derives from water through an H-enriched surface reservoir.



a, Ball-and-stick scheme: water (O, red; H, white) delivers hydrogen to a surface adsorbed-hydrogen (H_{ad}) reservoir, from which CD_x units are proposed to insert into the growing chain. **b**, In D_2O with ^{13}C-thiocyanate, ethylene appears predominantly at m/z 34 ($^{13}C_2D_4$), a single molecule carrying both the thiocyanate carbon and the water hydrogen. **c**, HCN is dominated by m/z 28–29 (^{13}C together with D), so the CN fragment carries thiocyanate carbon and water hydrogen. **d**, Products are near-completely deuterated in D_2O (H_2O reference at m = 0). **e**, Deuterium per carbon across the C_3–C_7 products: close to 2, the value for fully deuterated alkenes (88–97% of the maximum for C_4–C_6); the alkanes, whose maximum is 2 + 2/n, fall further below it. **f**, In 50:50 H_2O/D_2O the deuterium distribution is described by a per-site kinetic isotope effect of 5–7 (distribution fits; 4–8 from the mean D), far above the bulk rate value (1.3–1.4) and far below the no-KIE binomial, consistent with an H-enriched surface reservoir. **g**, C_5H_{10} isotopologue map across conditions (mass shift = ^{13}C + D). **h,** Share of the all-^{12}C isotopologue across the product slate: below 2% for most C_4 and larger products (at most 5%, C_7H_{14}) and larger only in the smallest products, whose clusters overlap other ions. **i**, The chain-growth probability is isotope-independent (α = 0.320 in H_2O, 0.321 in D_2O): consistent with an isotope-sensitive monomer-supply step, although similar isotope effects on propagation and termination remain possible. Error bars, range of duplicate electrolyses; deuteration distributions (single labelling runs), s.d. of a Poisson bootstrap over the measured ion counts. Full analysis in Supplementary Notes S7 and S14 (S14.3 and S14.11) and Supplementary Figs S72–S80 and S104–S106, consolidated in Supplementary Figs S107 and S108.

Active C–S and C–Se donors

We compared four precursors under identical conditions (Supplementary Notes S6 and S14). Rates relative to KSCN (100%) were thiourea, $SC(NH_2)_2$, 24%; KSeCN, 17%; and KOCN, 0.5%. KSCN and KOCN are isostructural (X–C≡N) and differ only in the chalcogen, yet the C–S compound is ≥200 times more active (the KOCN products are at the detection limit). Cyanate is expected to lose its carbon as CO_2 on hydrolysis. Thiourea, a C=S donor with no C≡N group, is also active, so a C≡N group is not required; the active donors share a reducible C–S or C–Se bond, whereas the C–O bond of cyanate (oxygen is also a chalcogen) does not deliver carbon (Fig. 1c). The series does not separate the reducibility of the C–X bond from the precursor's affinity for iron, and cyanide itself was not tested, so the series supports a working hypothesis for choosing donors rather than a rule. In 0.1 M bicarbonate, which gives the same C_1–C_7 slate (α = 0.34), the halides KF, KCl, KBr and KI each give only 0.07–0.12 μmol cm^{-2} h^{-1}, indistinguishable from the blank, so anion adsorption alone cannot explain the activity (Supplementary Note S8).

Apparent onset, pH and light

Between −0.6 and −1.8 V (applied) the chain-growth probability rises from 0.12 at −0.6 V, a value from products near the detection limit, to a constant ≈0.32 from −0.8 V onward; a logistic fit places an apparent onset at −0.64 V, whereas methane forms at every potential (Supplementary Note S4). Raising the bulk pH from 6.74 to 7.91 halves the rate (0.48×) at unchanged α (0.320 and 0.330)[25,26] (Supplementary Note S5), although the interfacial pH is set by hydroxide generation rather than by the bulk buffer (Supplementary Note S9). Illumination raises the hydrocarbon rate ≈2.4× but hydrogen only 1.2×. None of these variables changes α (Fig. 1f–h).

Impedance separates electrolyte heating

We examined the interface by voltammetry and operando impedance in four conditions (fifteen spectra each over an hour; Fig. 4; Supplementary Notes S16–S27)[27]. Voltammetry places this onset inside the accessible window (Fig. 4a). Thiocyanate leaves the current untouched at the onset (1.03× at −0.6 V_{RHE}) but suppresses it by 16–20% beyond −1.0 V, consistent with an adsorbed blocking layer. Over the ohmic-dominated branch $E = E_{on} - |I|R$ holds with $R^2 > 0.996$,

and light shifts the extrapolated onset by +135 mV in plain buffer and +86 mV with thiocyanate while leaving the slope unchanged to within 1.4% (Fig. 4b); this shift alone reproduces the measured current gain (+15.5% predicted, +14.2% measured). The shift is larger without thiocyanate, so it is not specific to an iron–thiocyanate chromophore, and because the current is mostly hydrogen evolution these measurements describe the interface, not the hydrocarbon channel.

Two time constants are resolved between 10 Hz and 1 MHz (Fig. 4c). The 1 MHz–50 kHz arc is assigned to the cell, giving R_u = 20–24 Ω, and the arc with its apex at 110–325 Hz to charge transfer. Thiocyanate in the dark halves the double-layer capacitance (153 → 81 μF cm^{-2}) and shortens the interfacial relaxation time ($R_{ct}C_{dl}$) from 0.75 to 0.47 ms without changing R_u (Fig. 4d), consistent with an adsorbed layer[28].

As illumination warms the electrolyte, R_u serves as a thermometer of the bulk electrolyte: ionic conduction is thermally activated, so $\ln(R_u/\Omega) = E_a/RT$ + constant is linear in 1/T (R^2 = 0.990 and 0.995), recovering the logged temperature of the same series to 0.2–0.3 K (in-sample), with activation energies (15.2 ± 0.8 and 16.6 ± 0.6 kJ mol^{-1}) typical of aqueous conduction (Fig. 4f; Supplementary Table S21). Retrospectively, a single 10 kHz point would give the temperature to 0.5 K, and three frequencies the interfacial relaxation time within ≈0.1 s (Supplementary Note S44).

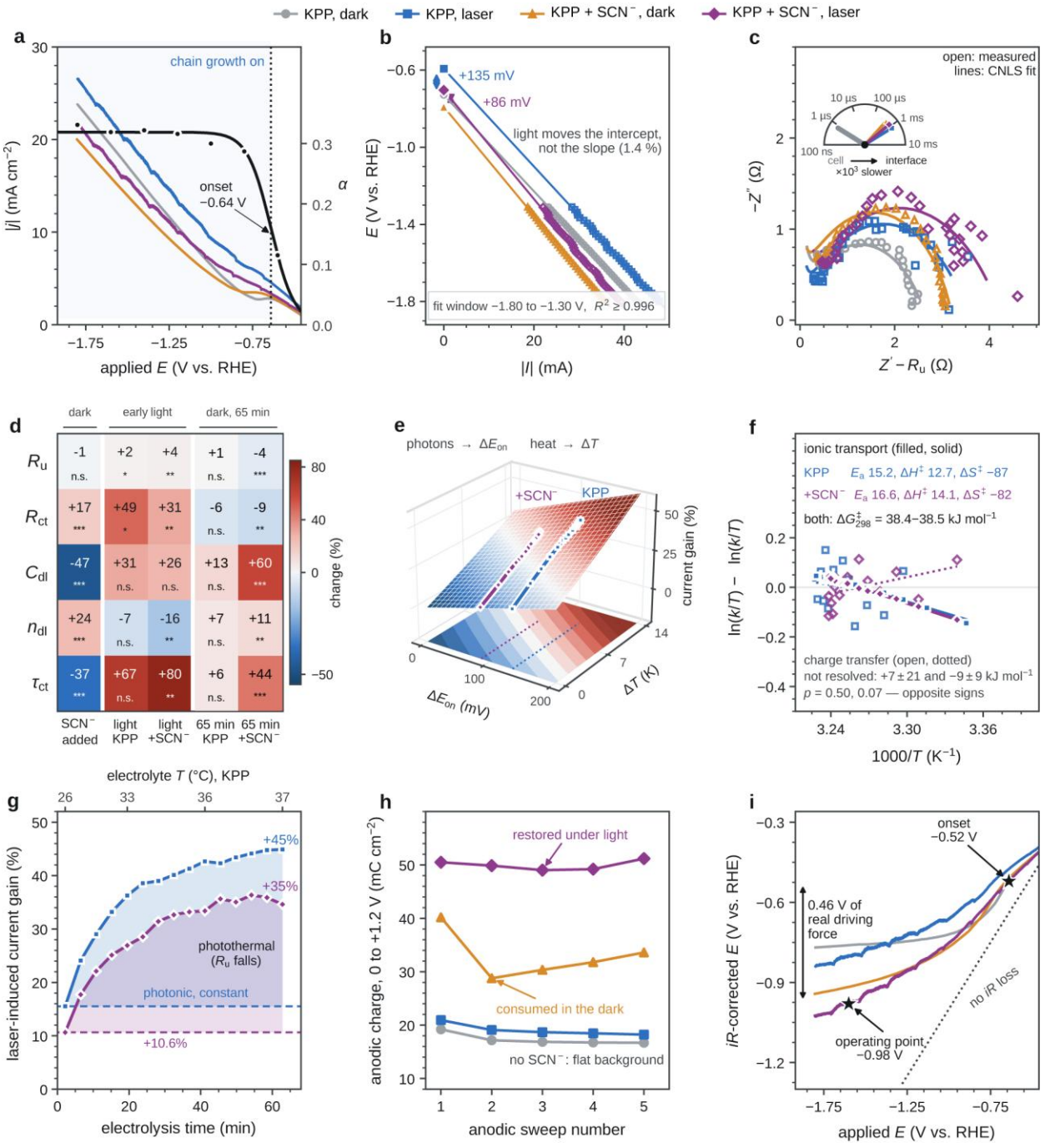
The enhancement then separates into two factors on different timescales (Fig. 4e,g). The photonic term (which may include heating of the illuminated spot) is the onset shift, taken as constant at +15.5% (plain buffer) and +10.6% (with SCN^-); the photothermal term is the bulk heating read from the fall in R_u relative to the first illuminated spectrum, growing to +25% and +22% as the electrolyte warms to 37 °C over an hour; the ≈3–4 K of warming before that spectrum (≈6–8% by the same calibration) is not included. Their product, modelled with R_{ct} at its dark value, takes the total gain from +16% to +45% and from +11% to +35%. Separating thermal from non-thermal effects requires independent temperature measurement[29–32]; R_u gives the bulk temperature in situ (Supplementary Note S28) but not that of the electrode surface under the beam. One contribution it cannot isolate is photoinduced reorientation of interfacial water, which laser pulses drive on model electrodes[33].

An anodic stripping feature at +0.15 to +0.25 V_{RHE} appears only with thiocyanate; it decays in successive dark sweeps but is restored under illumination (Fig. 4h; Supplementary Notes S18

and S24). This suggests that a sulfur-containing layer forms during electrolysis and re-forms faster under illumination.

The onset survives iR correction (Fig. 4i): 0.62–0.84 V is lost in the electrolyte at the operating bias, yet the operating point (−0.98 V from voltammetry; −0.81 V from the electrolysis current) lies 0.29–0.46 V beyond the onset (−0.52 V interfacial), so the onset is not an ohmic artefact (Supplementary Notes S9 and S29).

Fig. 4: Voltammetry and operando impedance resolve the potential onset and separate electrolyte heating from other light effects.



Four conditions are compared: 0.1 M potassium phosphate ± 0.25 mmol KSCN, dark and under 450 nm light. **a**, Current density against applied potential (left axis) with the chain-growth probability of Fig. 1f (right axis); the apparent logistic onset at −0.64 V is marked and the chain-growth region shaded. **b**, The ohmic-dominated branch, $E = E_{on} - |I|R$: illumination shifts the extrapolated onset by +135 mV (plain buffer) and +86 mV (with thiocyanate) while leaving the slope unchanged to 1.4%. Open symbols, points in the fit window (−1.80 to −1.30 V_{RHE}, $R^2 \geq 0.996$); filled markers, E_{on}. **c,** Low-frequency (charge-transfer) arc of a representative spectrum per condition after subtracting R_u: open symbols, measured (10 Hz–5 kHz); lines, circuit fit; grey crosses, Kramers–Kronig-rejected

points. Inset: the two relaxation times on a logarithmic scale: cell 0.8 μs, interface 0.47–1.32 ms ($R_{ct}C_{dl}$). **d**, Change in each interfacial parameter on adding thiocyanate (dark), early in illumination (first three retained illuminated spectra against the dark series, R_u temperature-corrected; two-sided Mann–Whitney U, n = 3 versus 14–15) and as drift over 65 min of dark electrolysis (linear-regression endpoints; p for the slope; n = 14 and 15); *** $p < 0.001$, ** $p < 0.01$, * $p < 0.05$. Each condition is one electrolysis, so p describes within-run consistency. **e**, Current gain over the photonic (onset shift) and photothermal (electrolyte warming) axes, with the 65-min trajectories of both electrolytes. **f**, Eyring analysis of each illuminated series (effective parameters of the cell RC response): ionic transport (filled) and charge transfer (open). **g**, The laser-induced current gain against time, referenced to the first illuminated spectrum and decomposed with R_{ct} at its dark value into the photonic term (dashed; light-associated, local heating not excluded) and the photothermal term that grows as R_u falls (shading). **h**, Anodic charge between 0 and +1.2 V_{RHE} over five successive voltammetric sweeps. **i**, iR-corrected potential (voltammetric currents) against applied potential, with the onset and the operating point starred. Details in Supplementary Notes S16–S29 and Figs S109–S119.

An oxidised, sulfur-bearing surface

Thiocyanate electrolysis produces crumpled flake- and sheet-like nanostructures that densify under illumination; without thiocyanate only rounded granular particles form (Supplementary Notes S30 and S31). Sulfur is detected by X-ray photoelectron spectroscopy only when thiocyanate is supplied; its chemical state was not assigned, because sulfide oxidised during air transfer cannot be distinguished from sulfate. Nitrogen appears at a similar level without thiocyanate and is adventitious rather than retained CN, consistent with the cyanide fragment leaving as gas-phase HCN and cyanogen.

The dominant surface component is nonetheless oxidic. X-ray diffraction shows only α-Fe, with a texture change from the pristine foil ((200)/(110) ≈6.9) to 0.69–0.82 on all reacted electrodes (Supplementary Note S32); Raman spectra are dominated by iron oxide and oxyhydroxide bands that would mask mackinawite (Supplementary Note S33); and after reaction the Fe 2p, O 1s and valence regions are those of an oxidised, sulfur-bearing surface (Supplementary Note S34) and the work function rises from 3.9 to 4.6–4.8 eV (Supplementary Note S35). Sulfur is thus incorporated into a predominantly oxide surface rather than forming a bulk sulfide (Supplementary Note S36). The amount retained is small: at $\sim 10^3$ carbons per surface iron atom per hour, most of the sulfur released by C–S scission must leave the electrode, probably as HS^-/H2S (Supplementary Notes S2 and S26).

Metals and calculations

All eight metals screened under the standard condition gave a full C_1–C_7 slate. Rates spanned nearly sevenfold (Fe > Cu > Ni > Ag > Co > Au > Pt > W), whereas α varied only between 0.27 and 0.36 (Fig. 5c)[34]. That metals with very different computed binding (Fig. 5a,f) all give this

slate suggests chain growth on a similar sulfur-modified surface, with metal-specific steps setting the rate.

We screened eleven transition-metal surfaces with a universal machine-learning interatomic potential. Four descriptors were evaluated on *SCN-modified surfaces: hydrogen and SCN adsorption energies and the largest step energies along the CO_2- and SCN-derived pathways. With equal weighting they rank Fe(110) first, as do the experiments (Fig. 5a; Supplementary Notes S37–S39), but across the eight metals the correlation is not significant (Pearson r = 0.64, p = 0.09; Fig. 5b; Supplementary Note S40), a known limitation of simple descriptor models[35].

Density functional theory on five surfaces resolves the individual steps. Along the SCN-derived pathway (∗C → ∗CH → ∗CH_2, then C–C coupling to ∗C_2H_4) every hydrogenation is downhill on all five surfaces and only the coupling step is uphill (Fig. 5d; Supplementary Note S41): +1.4 eV on Fe(110) and +0.5 to +2.1 eV on Ni, Ti and Pt, downhill on Cu(111). On copper the difficulty lies upstream: complete dissociation of ∗SCN into co-adsorbed S, C and N is endergonic on Cu(111) (ΔG_{diss} = +0.79 eV) but exergonic on Fe(110) (−0.23 eV), while Ni(111) and Ti(0001) over-dissociate SCN (−3.46 and −8.41 eV), which would favour chalcogen accumulation (Fig. 5f; Supplementary Note S42). These are overall reaction free energies, not the individual C–S and C–N steps or their barriers. Only iron and platinum (−0.39 eV) fall between these extremes; platinum, among the least active metals, probably loses to hydrogen evolution. Along the CO_2 pathway, CO_2 adsorption with ∗SCN present is endergonic on Cu, Ni and Pt, every step from ∗CO onward is downhill on Fe, Cu, Ni and Pt, and Fe shows the largest drop on forming ∗CH (Fig. 5e).

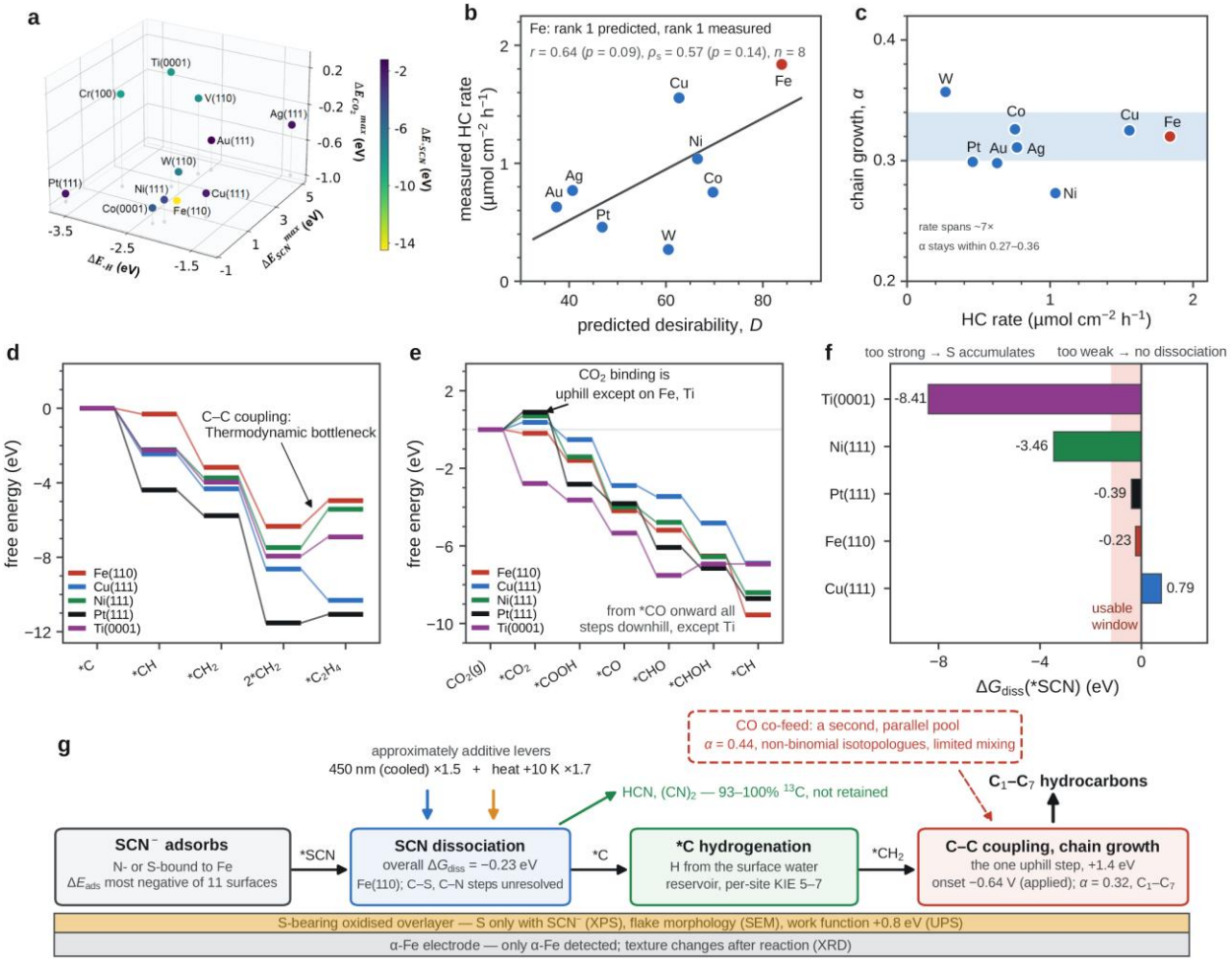
Proposed mechanism

Fig. 5g summarises the proposed pathway. Reductive C–S scission (complete dissociation of ∗SCN is slightly exergonic on Fe(110)), accelerated by illumination and mild heating, leaves sulfur on the surface and a CN fragment. Each CN fragment follows one of two branches: C–N scission gives surface carbon for chain growth, with the nitrogen leaving as ammonia, whereas fragments that keep the C–N bond leave as HCN (from which cyanogen can form at the anode) or, after reduction, as methylamine (^{1}H NMR; Supplementary Note S2). The carbon is hydrogenated from water-derived adsorbed hydrogen, and the CH_x monomers couple to chains above an apparent onset of −0.52 V (interfacial) with $\alpha \approx 0.32$ (Supplementary Note S29). In the

calculations C–C coupling is the only uphill step, thermodynamically (no barriers were computed, so it is not identified as rate-determining); as a chemical step, its free energy is potential-independent in the computational hydrogen electrode model, so the calculations do not explain the onset (Supplementary Note S41).

Thiocyanate supply, light, heat, pH and the choice of metal change the rate more than tenfold while α stays near 0.32 (Fig. 1i), suggesting that they act on monomer supply and that chain growth is set by the sulfur-modified surface. Thiocyanate is present in large excess (5.0 mM; ≈1.6% incorporated into hydrocarbons per hour; Supplementary Note S2) and the rate is nearly zero-order in it over 2–50 mM (in bicarbonate), as expected for a saturable surface complex rather than a diffusion-limited supply (Supplementary Note S8).

Fig. 5: Machine-learning screening, first-principles energetics and the integrated mechanism.



a, The eleven transition-metal surfaces in the descriptor space used for the screen: hydrogen adsorption energy, the largest elementary-step reaction energy along the SCN-derived and the CO_2 pathway, and, in colour, the ∗SCN adsorption energy. Iron receives the highest combined score, mainly through weak hydrogen binding and the strongest thiocyanate binding of the set. Ranking in Supplementary Table S30. **b**, Predicted desirability against the measured hydrocarbon rate for the eight metals tested; Fe is ranked first by both (Pearson r = 0.64, p = 0.09; Spearman ρ = 0.57, p = 0.14; n = 8; two-sided). **c**, Chain-growth probability against hydrocarbon rate across the metal screen: the rate spans nearly sevenfold while α stays within 0.27–0.36. **d**, Free-energy profile for hydrogenation and C–C coupling of SCN-derived ∗C; the coupling step is the only uphill step on four of the five surfaces (none is uphill on Cu). **e**, Free-energy profile for CO_2 reduction in the presence of ∗SCN; initial CO_2 binding is uphill except on Fe and Ti, while everything from ∗CO onward is downhill except one step on Ti(0001). **f**, Free energy of complete dissociation of ∗SCN into co-adsorbed S, C and N (C–S and C–N steps not resolved); iron and platinum fall between unfavourable dissociation (Cu) and sulfur accumulation (Ni, Ti), and only iron also ranks high on the combined descriptors. g, The proposed mechanism. Thiocyanate adsorbs on iron; light and heat accelerate C–S scission approximately additively; sulfur is retained in the surface overlayer and the CN fragment either loses nitrogen to give surface carbon or leaves as HCN or methylamine; water supplies hydrogen through an adsorbed reservoir; and C–C coupling is the only endergonic step in the calculated pathway (no kinetic barriers were computed); α ≈ 0.32 is observed above an apparent potential onset that the calculations do not reproduce. A CO co-feed opens a second, parallel pool. Bands beneath the sequence summarise the ex-situ characterisation (Supplementary Notes S30–S36, Figs S120–S124); computational details are in Supplementary Notes S37–S42 and Figs S125–S128.

Discussion

These results show that the surface carbon of aqueous electrochemical Fischer–Tropsch synthesis can come from a dissolved anion rather than from CO or CO_2, most plausibly through reductive C–S cleavage. The data point to a CN fragment whose C–N scission supplies the carbon, with part of the sulfur retained in the surface. The evidence is the SCN^--dependent switch-on, the ^{13}C and D labelling, the non-binomial ^{13}C signature under CO, the precursor series and the thiocyanate-specific surface sulfur; the reaction also proceeds on eight metals.

Because α stays near 0.32 above the apparent onset, the rate can be changed without changing chain length. The hydrocarbon Faradaic efficiency is ≈1.5%, 29–41% of the charge is not assigned to a detected product, the electrolyses lasted 1 h in an undivided cell, and HCN and cyanogen form alongside the hydrocarbons; dissolved sulfide and cyanide were not quantified (Supplementary Notes S24, S26 and S43). The carbon-source assignment rests most directly on ^{13}C labelling of the C_4–C_6 products; the efficiency is that of an unmodified foil, and a divided-cell control would test anodic contributions. A photo/dark enhancement factor depends on measurement time and thermal control, whether for a photothermal iron catalyst[36] or a pulsed-laser-driven surface[37].

The chemistry is reminiscent of the iron–sulfur world hypothesis for the origin of metabolism, in which iron-sulfide surfaces fix and couple carbon under mild aqueous conditions[38–40], and the light enhancement parallels reports of photo-promoted FeS carbon fixation[41]. For synthesis, the work separates carbon delivery from chain growth: a dissolved donor replaces the gas feed and builds chains to C7, and the precursor series indicates which bonds qualify. Thiourea and selenocyanate already qualify; other soluble C–S and C–Se donors, including waste-stream thiocyanate, are candidates if the chalcogen and nitrogen fragments can be managed. Liquid feeds, including carbon now destroyed as waste, then become usable.

Methods

Preparation of electrodes

Fe, Co, Ni, Cu, Ag, Au, Pt, and W metal sheets (99.99%; 0.1 mm thickness; AliExpress) were cut into pieces measuring 5 × 30 mm. Both sides of each metal sheet were mechanically abraded approximately 60 times using 2000-grit sandpaper to remove surface contamination. The

electrodes were subsequently ultrasonicated in deionised water for 10 min and dried under a stream of clean air.

Electrochemical CO and CO_2 reduction experiments

CO and CO_2 reduction experiments were conducted in a single-compartment three-electrode cell (total volume 122.5 mL, 50 mL of electrolyte). A CHI660D potentiostat (CH Instruments) was used for electrochemical measurements. The metal foil served as the working electrode, while a Pt coil and an Ag/AgCl reference electrode (sat. KCl) were used as the counter and reference electrodes, respectively. The cell was undivided, so species formed at the Pt anode (for example, by oxidation of thiocyanate or cyanide) can reach the cathode (Supplementary Note S43). HCN and cyanogen were detected in the headspace only; both are highly water-soluble, so their headspace amounts underestimate their formation, and they were not quantified. Electrolytes were prepared using $KHCO_3$ (99.7%, Sigma-Aldrich), $NaHCO_3$ (99.7%, Sigma-Aldrich), K_2HPO_4 (99.0%, Junsei), and KH_2PO_4 (99%, Acros). For additive experiments, 0.25 mmol of KSCN (99%, Yakuri), $SC(NH_2)_2$ (99%, Sigma-Aldrich), KSeCN (97%, Sigma-Aldrich), KOCN (96%, Sigma-Aldrich), or NaSCN (98%, Sigma-Aldrich) was added to the electrolyte. Before each experiment, the cell was purged with Ar (99.999%), CO (99.95%), or CO_2 (99.999%) for 10 min and then hermetically sealed, so that each electrolysis ran as a closed batch with no gas flow; HCN, cyanogen and H_2 therefore accumulate in the sealed headspace.

Amperometric *i–t* measurements were performed for 1 h at fixed potentials ranging from −1.19 to −2.39 V versus Ag/AgCl. The total electrode length immersed in the electrolyte was fixed at 1.8 cm from a 3.0 cm total electrode length, giving a geometric area of 1.8 cm^2 based on 5 × 18 mm of exposed electrode area on each face. The applied potentials were converted to the RHE scale using the Nernst equation: $V_{RHE} = V_{Ag/AgCl} + (0.0592 \times pH) + 0.197$.

The measured pH values for the different gas and electrolyte conditions are provided in the Supplementary Information.

For isotope-effect experiments conducted in D_2O, the potential conversion was modified according to: $V_{RHE} = V_{Ag/AgCl} + (0.0592 \times pD) + 0.197$. The Nernst slope 2.303RT/F depends on temperature and not on the hydrogen isotope, so the same factor is used in H_2O and in D_2O, both series having been run under the same temperature conditions. The H_2/H^+ and D_2/D^+ reference potentials differ and are not corrected on this scale, so the H_2O/D_2O rate ratios are apparent

isotope responses at nominal potential, not corrected to a common interfacial overpotential. For the pH-series experiments, phosphate buffers were prepared by mixing KH_2PO_4 and K_2HPO_4 stock solutions in different ratios; for example, the basic buffer (0.1 M total phosphate) was prepared by mixing 0.5 mL of 1 M KH_2PO_4 and 4.5 mL of 1 M K_2HPO_4, followed by dilution with 45.0 mL of distilled water.

Isotope-effect experiments were performed to further investigate the reaction mechanism. In these experiments, D_2O (99.8 atom% D, Thermo Scientific) was used as the solvent, while all other experimental procedures and conditions were kept identical to those used in the standard experiments, which were carried out at room temperature. For the halide-series experiments, 0.25 mmol of potassium halide (KX, X = F, Cl, Br, or I) was added. The halide salts used were KF (99%, Thermo Fisher), KCl (99.99%, Sigma-Aldrich), KBr (99%, Daejung), and KI (99.5%, Samchun).

Photothermal experiments

Photothermal effects were investigated using laser irradiation with a LaserPecker LP2 laser system (450 nm, 5 W, 50 μm spot size). Laser parameters, including the output power and depth settings, were controlled using the manufacturer-provided software. The standard irradiation conditions were 100% power (5 W), depth 10, and a scan speed of 39.5 mm s^{-1}. The laser beam was raster-scanned over the 5 × 18 mm exposed face of the electrode at a source-to-electrode distance of 11 cm. With a 50 μm line pitch, one raster pass (100 lines of 18 mm) takes ≈46 s at 39.5 mm s^{-1}, so the beam was rastered continuously for ≈79 passes over the 1 h electrolysis, giving a time-averaged nominal irradiance of ≈5.6 W cm^{-2} on the 0.9 cm^2 illuminated face. The same geometry was used in every illuminated experiment. To examine the thermal contribution to the reaction kinetics, the electrochemical cell was placed in a constant-temperature water bath maintained at 308 K. This temperature was selected to match the electrolyte temperature measured during laser irradiation, allowing comparison between the photothermal and purely thermal effects. For the photochemical control the illuminated cell was instead held in an ice bath, keeping the electrolyte near 20 °C.

Electrochemical measurements

Linear sweep voltammetry (LSV) and cyclic voltammetry (CV) were performed using a CHI 660D potentiostat (CH Instruments). LSV measurements were conducted at a scan rate of 10 mV s^{-1} over a potential range of 0.6 to −1.8 V_{RHE} under both dark and laser-irradiation conditions, with and without SCN^-. CV measurements were performed between −0.9 and 2.1 V_{RHE} at a scan rate of 50 mV s^{-1}. These voltammetric measurements were conducted under the various experimental conditions examined in this study.

Operando impedance measurements

Potentiostatic impedance spectra were acquired over a frequency range of 1 MHz to 0.1 Hz using a 5 mV perturbation amplitude at −1.6 V_{RHE}. Fifteen consecutive spectra were collected for each condition during 65 min of continuous polarisation, and for the illuminated series the electrolyte temperature was recorded after each spectrum. Before equivalent-circuit fitting, the spectra were evaluated against the Kramers–Kronig relations using a linear measurement model[42]. The spectra were then fitted over the frequency range from 1 MHz to 10 Hz by complex nonlinear least-squares fitting with modulus weighting using the equivalent circuit $R_{ser} + (R_{HF} \parallel CPE_{HF}) + (R_{ct} \parallel CPE_{dl})$. Double-layer capacitances were calculated as Brug effective capacitances[43]. Relaxation-time distributions were obtained by Tikhonov-regularised deconvolution[44] and were used only as a model-free cross-check of the number of time constants. The rejection criteria, equivalent-circuit selection, and complete parameter set are provided in Supplementary Notes S16–S27. The fitted equivalent-circuit model was used to obtain the kinetic descriptors.

Computational methods: machine-learning potential and density functional theory

Candidate surfaces were screened with the universal machine-learning interatomic potential UMA (uma-s-1p2) through the FAIRChem calculator in OC20 task mode[45,46], with structures built, constrained and relaxed using the Atomic Simulation Environment[47]. Eleven low-index transition-metal surfaces were modelled as 4 × 4 × 1 slabs with the two bottom layers fixed, and four descriptors were evaluated on ∗SCN-modified slabs: the hydrogen and the SCN adsorption energies and the largest elementary-step reaction energy along the CO_2- and the SCN-derived pathway. Periodic density functional theory on five representative surfaces was performed with

VASP using projector augmented-wave potentials[48] and the PBE functional[49] with a 400 eV plane-wave cutoff, and free energies of the electrochemical steps were obtained within the computational hydrogen electrode approximation[50]. Slab models, descriptor definitions, the desirability score and the optimised geometries are given in Supplementary Notes S37–S42.

Analysis of reduction products

Gas- and liquid-phase products were collected following 1 h of amperometric electrolysis and analysed by gas chromatography (GC) and nuclear magnetic resonance (NMR) spectroscopy, respectively. Gas-phase products were quantified using a YL 6500 GC system equipped with thermal conductivity (TCD) and flame ionisation (FID) detectors with a Ni-catalyst methanizer. H_2, CO, CH_4, and C_2 compounds were separated using a 40/60 Carboxen-1000 column, whereas C_3–C_7 compounds were identified using an HP Plot Q PT column.

Production rates, expressed in μmol cm^{-2} h^{-1}, included all detected products, including H_2, whereas Faradaic efficiencies were reported for carbon-containing products. The Faradaic efficiency of each product was calculated according to: $FE = \{nZF / (I \times t)\} \times 100\%$, where n is the molar amount of the product determined by GC, Z is the number of electrons transferred (2a + b for C_aH_b from thiocyanate, a lower bound; Supplementary Note S14), F is the Faraday constant (96,485 C mol^{-1}), I is the average current obtained from the amperometric measurement, and t is the reaction time. Each value is the mean of two independent electrolyses, and error bars show the range of the two runs (mean ± half their difference), propagated to derived quantities; with n = 2 no standard deviation is given. The standard condition (Ar, KSCN, −1.6 V_{RHE}, 450 nm) was measured as one duplicate pair that serves as the reference in each series. The metal screens, the D_2O series, the ^{13}C-labelling experiments and parts of the bicarbonate series are single electrolyses, for which no run-to-run uncertainty is given (Supplementary Note S43).

The chain-growth probability, α, was determined from the Anderson–Schulz–Flory slope fitted to the C_2–C_7 products, with C_1 excluded from all fits. The uncertainty in α was calculated as the standard error of the fitted slope.

For isotopic tracing of hydrocarbon products, gas chromatography–mass spectrometry (GC-MS) was performed using a Shimadzu GCMS-QP2020 NX system operated in electron ionisation (EI) mode. A 1 mL aliquot of the headspace gas was injected using a gas-tight syringe,

and mass spectra were acquired in full-scan mode (recorded spectra m/z 20–200, 0.5 s per scan). C_3–C_6 hydrocarbon isotopologues were qualitatively identified using the NIST14 and NIST14s libraries and further cross-confirmed by matching retention times with a reference map.

Liquid-phase products were analysed using a 600 MHz FT-NMR spectrometer (AVANCE III, Bruker Corp.). For NMR analysis, 0.5 mL of electrolyte was mixed with 0.1 mL of an internal-standard solution (maleic acid in DMSO/D_2O) in 5 mm NMR tubes (WG-1241-7, Wilmad-LabGlass).

Characterisation of electrodes

The crystal structures of the electrodes were examined by X-ray diffraction (XRD; Rigaku MiniFlex II) using Cu Kα radiation (λ = 1.5418 Å) at the CNU Chemistry Core Facility. The surface morphology of Fe electrodes before and after electrolysis was investigated by scanning electron microscopy (SEM; Hitachi S-4800) using a probe current of 10 μA and an accelerating voltage of 10 kV with secondary-electron detection. The interfacial electronic structures of the electrodes before and after electrolysis were analysed by X-ray photoelectron spectroscopy (XPS; Thermo Scientific K-alpha$^+$) using monochromatic Al Kα radiation with a 100 μm spot size and a photon energy of 1486.7 eV. High-resolution spectra of Fe 2p, C 1s, O 1s, N 1s, S 2p, P 2p, and the valence band were acquired. Valence-band spectra were collected at a pass energy of 40 eV with 20 scans and a step size of 0.1 eV, while core-level spectra were collected at a pass energy of 50 eV with 5 scans and a step size of 0.1 eV. A low-energy electron flood gun was used to compensate for charging effects. The work function and valence band were measured before and after electrolysis by ultraviolet photoelectron spectroscopy (UPS; Thermo Scientific Nexsa G2, He I, 21.22 eV, 5 eV pass energy). Raman spectra were acquired with 633 nm excitation.

Isotopologue data analysis

Carbon tracing was performed using ^{13}C-labelled KSCN (99 atom% ^{13}C, Sigma-Aldrich), while hydrogen tracing was conducted using D_2O. The two isotope labels were used separately and in combination under Ar and under CO or CO_2 co-feed conditions. Molecular-ion clusters were deconvoluted to obtain isotopologue distributions and compared with the binomial distribution expected from a single, fully mixed monomer pool. Because each labelling experiment is a single

electrolysis, the uncertainties of the deconvoluted isotopologue fractions were estimated by Poisson bootstrap resampling of the measured ion counts; they reflect counting statistics only, not run-to-run variation. Molecular-ion and fragment isotope envelopes, together with branched-isomer distributions, were used as supplementary cross-checks (Supplementary Notes S10–S15); the fragment comparison does not resolve carbon positions within a chain. Apparent pH values measured in D_2O were converted to pD using the standard glass-electrode correction described in Supplementary Note S5. For runs with unlabelled thiocyanate, the measured M^+ ion-intensity envelope of each product was deconvoluted against the natural-abundance ^{13}C distribution to obtain the deuteration distribution, D_k. The convolution matrix was constructed using the binomial ^{13}C distribution with $p = 0.0107$ per carbon. The system was solved by non-negative least squares with the constraint $D_k \geq 0$, followed by normalisation to 100%. For ^{13}C-thiocyanate in H_2O, each molecular-ion cluster was deconvoluted against the cluster of the same product from the unlabelled run, which contains its hydrogen-loss fragments and natural ^{13}C; the ^{13}C atom fraction was taken as $\Sigma_m\ m \cdot p_m/n$ and the thiocyanate-derived fraction as that value divided by the reagent enrichment (0.99). Widening the fragment window by one mass unit raises the values by at most 2 percentage points; narrowing it leaves part of the hydrogen-loss fragments unmodelled and lowers the C_4 values by 3–6 points (Supplementary Note S14.10).

From each distribution, the mean fractional deuteration, $f_D = \langle k \rangle / n_H$, was calculated together with the fully deuterated (D_n) and non-deuterated (D_0) populations, the D_{n-2} and D_1 populations, the excess of even deuteration relative to a binomial reference at the same f_D, and a two-pool (end-population) index. These are descriptive indices; because electron-ionisation fragments were not fully separated from them, they are not assigned to specific mechanisms. The same analysis procedure was applied to every product under every experimental condition, and all isotopologue figures were generated from these calculated quantities.

The deconvolution and the diagnostic metrics were computed with deterministic Python scripts, and their numerical outputs were checked by the authors against the raw GC–MS files.

Use of AI tools

A large language model (Claude, Anthropic) assisted with drafting analysis and plotting code (impedance fitting, GC–MS isotopologue analysis, Anderson–Schulz–Flory fitting and plotting) and with language editing. The authors specified the analysis procedures, checked numerical

outputs against the corresponding experimental data or calculation files, reviewed all interpretations and take responsibility for the final content. Data panels were rendered with these scripts (Matplotlib) from the measured data files; schematic panels were prepared under the authors' direction, and no generative image model was used; in accordance with Nature Portfolio policy, the model is not listed as an author. Further details are given in the Supplementary Information.

Data availability

The data supporting the findings of this study are available within the paper and its Supplementary Information. Raw instrument files (GC, GC–MS, voltammetry and impedance), the isotopologue deconvolution outputs and the computed structures are available from the corresponding authors upon request.

Code availability

The Python scripts used for the impedance analysis, the GC–MS isotopologue deconvolution (including the ^{13}C atom-fraction calculation), the Anderson–Schulz–Flory fitting, the machine-learning screening and the plotting of the figures are available from the corresponding authors upon request.

References

1. Nitopi, S. et al. Progress and perspectives of electrochemical CO_2 reduction on copper in aqueous electrolyte. *Chem. Rev.* **119**, 7610–7672 (2019).
2. Fan, L. et al. Atomic-level Cu active sites enable energy-efficient CO_2 electroreduction to multicarbon products in strong acid. *Nat. Synth.* **4**, 262–270 (2025).
3. Chen, Y. et al. Dilute alloy electrocatalysts enable asymmetric C–C coupling for ethylene production from a CO_2 post-capture liquid. *Nat. Synth.* **5**, 1111–1122 (2026).
4. Vos, R. E. et al. CO_2 electroreduction on Cu operates via an alternative chain-growth mechanism to form C–C bonds at elevated temperature and pressure. *Nat. Catal.* **8**, 1338–1347 (2025).
5. Rommens, K. T. & Saeys, M. Molecular views on Fischer–Tropsch synthesis. *Chem. Rev.* **123**, 5798–5858 (2023).

6. Ye, R. et al. Design of catalysts for selective CO_2 hydrogenation. *Nat. Synth.* **4**, 288–302 (2025).
7. Zhou, Y. et al. Long-chain hydrocarbons by CO_2 electroreduction using polarized nickel catalysts. *Nat. Catal.* **5**, 545–554 (2022).
8. Ou, Y. et al. Controlling hydrocarbon chain growth and degree of branching in CO_2 electroreduction on fluorine-doped nickel catalysts. *Nat. Catal.* **8**, 714–727 (2025).
9. Preikschas, P. et al. CO_2 electroreduction to long-chain hydrocarbons on cobalt catalysts. *Adv. Energy Mater.* **14**, 2401447 (2024).
10. Hwang, S. Y. et al. Electrochemical Fischer–Tropsch chemistry across transition metals: a paradigm shift in sustainable liquid fuel production. *Nano Energy* **128**, 109881 (2024).
11. Yang, J. H. et al. Exploring direct electrochemical Fischer–Tropsch chemistry of C_1–C_7 hydrocarbons via perimeter engineering of an Au–$SrTiO_3$ catalyst. *Adv. Energy Mater.* **14**, 2402062 (2024).
12. Hwang, S. Y., Yun, G., Yeo, B. S. & Sohn, Y. Electrochemical Fischer–Tropsch chemistry. *Chem. Eng. J.* **520**, 165806 (2025).
13. Zhang, Q. et al. Metal electrode potential diverges with ion additions. *Nat. Chem.* **18**, 1443–1450 (2026).
14. Huang, Y., Ong, C. W. & Yeo, B. S. Effects of electrolyte anions on the reduction of carbon dioxide to ethylene and ethanol on copper (100) and (111) surfaces. *ChemSusChem* **11**, 3299–3306 (2018).
15. Yoo, J. M., Ingenmey, J., Salanne, M. & Lukatskaya, M. R. Anion effect in electrochemical CO_2 reduction: from spectators to orchestrators. *J. Am. Chem. Soc.* **146**, 31768–31777 (2024).
16. Wang, F. et al. Thiocyanate “passivation” unlocks highly selective and efficient acidic CO_2 electroreduction to CH_4 on Cu-based catalysts. *J. Am. Chem. Soc.* **148**, 19283–19292 (2026).
17. Cao, P., Yao, J., Ren, B., Gu, R. & Tian, Z.-Q. Potential dependence of the orientation of thiocyanate adsorbed on an iron electrode as probed by surface-enhanced Raman spectroscopy. *J. Phys. Chem. B* **106**, 7283–7285 (2002).
18. Jiang, F. et al. Insights into the influence of support and potassium or sulfur promoter on iron-based Fischer–Tropsch synthesis. *Catal. Sci. Technol.* **7**, 1245–1265 (2017).

19. Fedurco, M., Jorand Sartoretti, C. & Augustynski, J. Electrochemical conversion of cyanide into methylamine and C_1–C_2 hydrocarbons. *J. Am. Chem. Soc.* **121**, 888–889 (1999).
20. Johansen, C. M. & Peters, J. C. Catalytic reduction of cyanide to ammonia and methane at a mononuclear Fe site. *J. Am. Chem. Soc.* **146**, 5343–5354 (2024).
21. Zhang, J. et al. Isotopic labelling of water reveals the hydrogen transfer route in electrochemical CO_2 reduction. *Nat. Chem.* **17**, 334–343 (2025).
22. Liu, P. et al. Electrosynthesis of ethanol via CO–CH_x cross-coupling on copper alloy catalysts with engineered oxygen affinity. *Nat. Synth.* **4**, 1462–1472 (2025).
23. Zhang, H., Raciti, D. & Hall, A. S. Disordered interfacial H_2O promotes electrochemical C–C coupling. *Nat. Chem.* **17**, 1161–1168 (2025).
24. Jackson, M. N., Jung, O., Lamotte, H. C. & Surendranath, Y. Donor-dependent promotion of interfacial proton-coupled electron transfer in aqueous electrocatalysis. *ACS Catal.* **9**, 3737–3743 (2019).
25. Kastlunger, G. et al. Using pH dependence to understand mechanisms in electrochemical CO reduction. *ACS Catal.* **12**, 4344–4357 (2022).
26. Ledezma-Yanez, I. et al. Interfacial water reorganization as a pH-dependent descriptor of the hydrogen evolution rate on platinum electrodes. *Nat. Energy* **2**, 17031 (2017).
27. Vivier, V. & Orazem, M. E. Impedance analysis of electrochemical systems. *Chem. Rev.* **122**, 11131–11168 (2022).
28. Hou, J., Xu, B. & Lu, Q. Influence of electric double layer rigidity on CO adsorption and electroreduction rate. *Nat. Commun.* **15**, 1926 (2024).
29. Zhou, L. et al. Quantifying hot carrier and thermal contributions in plasmonic photocatalysis. *Science* **362**, 69–72 (2018).
30. Liu, C. et al. Micro/nanoscale thermometry in photothermal catalysis. *Joule* **9**, 102052 (2025).
31. Baffou, G., Bordacchini, I., Baldi, A. & Quidant, R. Simple experimental procedures to distinguish photothermal from hot-carrier processes in plasmonics. *Light Sci. Appl.* **9**, 108 (2020).
32. Geng, Z. et al. Achieving maximum overall light enhancement in plasmonic catalysis by combining thermal and non-thermal effects. *Nat. Catal.* **6**, 1241–1247 (2023).

33. García-Aráez, N., Climent, V. & Feliu, J. M. Evidence of water reorientation on model electrocatalytic surfaces from nanosecond-laser-pulsed experiments. *J. Am. Chem. Soc.* **130**, 3824–3833 (2008).
34. Kuhl, K. P. et al. Electrocatalytic conversion of carbon dioxide to methane and methanol on transition metal surfaces. *J. Am. Chem. Soc.* **136**, 14107–14113 (2014).
35. Kim, B. et al. Peaks and pitfalls of electrocatalytic CO_2 reduction descriptor models. *Nat. Catal.* **9**, 471–481 (2026).
36. Song, C. et al. Photothermal conversion of CO_2 with tunable selectivity using Fe-based catalysts: from oxide to carbide. *ACS Catal.* **10**, 10364–10374 (2020).
37. Baldi, A. & Askes, S. H. C. Pulsed photothermal heterogeneous catalysis. *ACS Catal.* **13**, 3419–3432 (2023).
38. Wächtershäuser, G. Before enzymes and templates: theory of surface metabolism. *Microbiol. Rev.* **52**, 452–484 (1988).
39. Huber, C. & Wächtershäuser, G. Activated acetic acid by carbon fixation on (Fe,Ni)S under primordial conditions. *Science* **276**, 245–247 (1997).
40. Russell, M. J. & Hall, A. J. The emergence of life from iron monosulphide bubbles at a submarine hydrothermal redox and pH front. *J. Geol. Soc. Lond.* **154**, 377–402 (1997).
41. Nan, J. et al. Iron sulfide-catalyzed gaseous CO_2 reduction and prebiotic carbon fixation in terrestrial hot springs. *Nat. Commun.* **15**, 10280 (2024).
42. Boukamp, B. A. A linear Kronig–Kramers transform test for immittance data validation. *J. Electrochem. Soc.* **142**, 1885–1894 (1995).
43. Brug, G. J., van den Eeden, A. L. G., Sluyters-Rehbach, M. & Sluyters, J. H. The analysis of electrode impedances complicated by the presence of a constant phase element. *J. Electroanal. Chem.* **176**, 275–295 (1984).
44. Wan, T. H., Saccoccio, M., Chen, C. & Ciucci, F. Influence of the discretization methods on the distribution of relaxation times deconvolution: implementing radial basis functions with DRTtools. *Electrochim. Acta* **184**, 483–499 (2015).
45. Wood, B. M. et al. UMA: a family of universal models for atoms. Preprint at https://arxiv.org/abs/2506.23971 (2025).
46. Chanussot, L. et al. Open Catalyst 2020 (OC20) dataset and community challenges. *ACS Catal.* **11**, 6059–6072 (2021).

47. Larsen, A. H. et al. The atomic simulation environment — a Python library for working with atoms. *J. Phys.: Condens. Matter* **29**, 273002 (2017).
48. Kresse, G. & Joubert, D. From ultrasoft pseudopotentials to the projector augmented-wave method. *Phys. Rev. B* **59**, 1758–1775 (1999).
49. Perdew, J. P., Burke, K. & Ernzerhof, M. Generalized gradient approximation made simple. *Phys. Rev. Lett.* **77**, 3865–3868 (1996).
50. Nørskov, J. K. et al. Origin of the overpotential for oxygen reduction at a fuel-cell cathode. *J. Phys. Chem. B* **108**, 17886–17892 (2004).

Acknowledgements

This work was supported by the National Research Foundation of Korea (NRF) grant funded by the Korea government (MSIT) (RS-2026-25472021; RS-2026-25590733) and by the BK21 FOUR Program of Chungnam National University (2025, 2026), and by the Chungnam National University Global Research Laboratory Program (CNU Global) for the international collaboration with the National University of Singapore.

Author information

Authors and Affiliations

Department of Chemistry, Chungnam National University, Daejeon, 34134, Republic of Korea

Hyeonji Lee, Hee Sub Yun, Huieun Shim, Jaehee Shin, Hee-Joon Chun & Youngku Sohn

Department of Chemical and Biomolecular Engineering, National University of Singapore, Singapore, Singapore

Lei Wang

Department of Chemistry, National University of Singapore, Singapore, Singapore

Boon Siang Yeo

These authors contributed equally: Hyeonji Lee, Hee Sub Yun.

Contributions

Conceptualisation: H.-J.C., Y.S., L.W. and B.S.Y. Methodology: H.L., H.S. and Y.S. Software: H.Y. Investigation: H.L., H.Y., H.S., J.S. and Y.S. Validation: H.S. Formal analysis: H.Y., H.-J.C. and Y.S. Data curation: H.L. Visualisation: H.-J.C. and Y.S. Writing – original draft: H.-J.C. and Y.S. Writing – review and editing: L.W., B.S.Y. and all authors. Supervision: H.-J.C. and Y.S., with partial supervision by L.W. and B.S.Y. Project administration: Y.S. Funding acquisition: H.-J.C. and Y.S.

Corresponding authors

Correspondence to Hee-Joon Chun or Youngku Sohn

Ethics declarations

Competing interests

The authors declare no competing interests.

Additional information

Supplementary Information is available for this paper. Correspondence and requests for materials should be addressed to H.-J.C. and Y.S.

Supplementary Files

This is a list of supplementary files associated with this preprint. Click to download.

- FeSCNSI.docx
- Graphicalabstract.tif